

Recombination Clumping Factor of Physically Defined Intergalactic Medium at the Epoch of Reionization

YURI OKU  ^{1,2} AND RENYUE CEN  ^{1,2}

¹Center for Cosmology and Computational Astrophysics, Institute for Advanced Study in Physics Zhejiang University, Hangzhou 310058, China

²Institute of Astronomy, School of Physics, Zhejiang University, Hangzhou 310058, China

ABSTRACT

The recombination clumping factor, C , is a key parameter in modeling cosmic reionization, but its value is sensitive to the definition of the Intergalactic Medium (IGM). We investigate the clumping factor using the GAMER adaptive mesh refinement cosmological hydrodynamical simulation code. We introduce a new, physically-motivated definition of the IGM based on the effective transmission factor of ionizing photons. We perform large-scale, full-box simulations with varying intensities of the uniform ultraviolet background, and we find that our physically-defined clumping factor is significantly lower than the values derived from traditional overdensity thresholds. We also introduce an analytic model that distinguishes between the volume-weighted and mass-weighted averages of the neutral fraction, and we find the difference in reionization timing of $\Delta z \sim 2$ depending on the assumed clumping factor and the relation between the volume-weighted and mass-weighted neutral fractions. Our zoom-in simulations further show that, while SN feedback increases the clumping factor locally, the effect is limited to ~ 100 kpc scales and does not significantly alter the global clumping factor. The substantially lower clumping factor reduces the required ionizing photon budget, potentially alleviating tension for reionization scenarios driven by rare, bright sources like active galactic nuclei.

Keywords: Intergalactic medium (813) — Reionization (1383) — Hydrodynamical simulations (767)

1. INTRODUCTION

The first galaxies in the universe emitted ionizing photons, which transformed the intergalactic medium (IGM) from a neutral state to an ionized state, a process known as cosmic reionization (for recent reviews, see B. E. Robertson 2022; N. Y. Gnedin & P. Madau 2022). The evolution of the IGM’s ionization state is governed by the balance between the rate at which ionizing photons are produced and the rate at which ionized hydrogen recombines. The classical model introduced by P. Madau et al. (1999) describes the filling factor of ionized hydrogen, Q_{HII} , as

$$\frac{dQ_{\text{HII}}}{dt} = \frac{\dot{n}_{\text{ion}}}{\langle n_{\text{H}} \rangle} - \frac{Q_{\text{HII}}}{\bar{t}_{\text{rec}}}, \quad (1)$$

where \dot{n}_{ion} is the production rate of ionizing photons per unit volume, $\langle n_{\text{H}} \rangle$ is the mean hydrogen number density, and \bar{t}_{rec} is the volume-averaged recombination time.

Because the recombination rate depends on the square of the local ionized gas density, it is highly sensitive

to the small-scale structure, or “clumpiness,” of the IGM. This clumpiness is commonly quantified by the clumping factor, defined as the ratio of the mean of the squared density to the square of the mean density, i.e., $C \equiv \langle n^2 \rangle / \langle n \rangle^2$ (N. Y. Gnedin & J. P. Ostriker 1997). The clumping factor has been refined over the decades, using simulations with higher resolution and more sophisticated physics, such as radiative transfer, as well as improving the formalism of the clumping factor by accounting for the spatial variation of the temperature (H. Trac & R. Cen 2007; K. Kohler et al. 2007; A. H. Pawlik et al. 2009; K. Finlator et al. 2012; J. M. Shull et al. 2012; G. C. So et al. 2014; A. A. Kaurov & N. Y. Gnedin 2015; N. Chen et al. 2020; R. Kannan et al. 2022).

However, the clumping factor remains sensitive to the adopted definition of the IGM. Since the clumping factor is intended to quantify recombination in the diffuse IGM, it is essential to exclude regions associated with galaxies. This avoids double-counting recombinations that are already accounted for in the escape fraction of ionizing photons from galaxies.

Another important aspect is the definition of the ‘ Q ’ in Eq. (1). Q is often interpreted as the vol-

ume fraction of ionized regions; however, the ionization and recombination rates account for the number of ionized hydrogen atoms in the IGM, which translates to the mass-weighted ionization fraction rather than the volume fraction. N. Chen et al. (2020) proposed a mass-weighted ionization fraction model, which is more physically consistent with the ionization and recombination rates. They also introduced a clumping factor definition that is consistent with the mass-weighted ionization fraction model, and demonstrated its effectiveness in reproducing the ionization history in their SCORCH radiation-hydrodynamic simulations. Although the mass-weighted ionization fraction model is more physically accurate, the volume fraction is commonly used in the literature, and we seek to translate the mass-weighted and volume weighted neutral fractions.

Lastly, the clumping factor and the relation between mass-weighted and volume-weighted ionization fractions depend on the topology of reionization, which is influenced by the nature of ionizing sources. Previous numerical works are limited to small-volume simulations with radiative transfer and/or adopted subgrid physics, which may not capture the influences from luminous sources, such as active galactic nuclei (AGNs). P. Madau et al. (2024) recently showed that the abundance of moderate-luminosity type 1 AGNs at $4 \lesssim z \lesssim 13$ detected by the James Webb Space Telescope (JWST) is enough to reionize the universe by $z \sim 5.3 - 5.5$ using analytical modeling. Their fiducial model assumes the type 1 AGN fraction of 15%, and there is no photon escape from galaxies that do not host AGNs. In such a scenario where rare sources dominate, the topology of reionization is expected to be outside-in, where underdense regions are ionized first (J. Miralda-Escudé et al. 2000), in contrast to the conventional inside-out reionization scenario driven by stellar sources in young galaxies (S. R. Furlanetto et al. 2004; S. R. Furlanetto & S. P. Oh 2005).

In this article, we present a physically motivated definition of the IGM based on the effective optical depth to ionizing photons from external sources, and we reformulate the recombination clumping factor accordingly. We also provide the relation between the mass-weighted and volume-weighted neutral fraction of hydrogen. Our cosmological hydrodynamical simulations adopt a uniform ultraviolet background (UVB) as the ionizing source, allowing us to study the reionization history and clumping factor of the IGM irradiated by external sources with high spatial resolution in a comoving simulation volume of $(20 \text{ Mpc}/h)^3$.

The remainder of this article is organized as follows. In Section 2, we present the physical definition of the IGM and the recombination clumping factor. In Section 3, we measure the clumping factor in large-volume cosmological simulations with different UVB intensities. In Section 4, we measure the clumping factor in zoom-in simulations that resolve small-scale structures in the IGM and discuss the feedback effects on the clumping factor. Finally, we summarize our findings and discuss their implications in Section 5.

2. RECOMBINATION CLUMPING FACTOR

The ionization balance of the diffuse IGM in a comoving volume of V is described by

$$\frac{dN_{\text{HII}}^{\text{IGM}}}{dt} = \dot{N}_{\text{ion}}^{\text{IGM}} + \int_{\text{IGM}} [\gamma_{\text{coll}} n_{\text{HII}} n_{\text{e}} - \alpha n_{\text{HII}} n_{\text{e}}] dv, \quad (2)$$

where $N_{\text{HII}}^{\text{IGM}}$ is the number of ionized hydrogen atoms in the IGM, \dot{N}_{ion} is the total photoionization rate in the comoving volume V , γ_{coll} is the collisional ionization coefficient, α is the recombination coefficient, and n_{HII} , n_{HI} , and n_{e} are the densities of ionized hydrogen, neutral hydrogen, and electrons, respectively.

Here, we define the diffuse IGM as the region traversed by the ionizing photons, i.e., not self-shielded by the neutral hydrogen. We also ignore collisional ionization, which is subdominant compared to photoionization in the low-density IGM. Then, the integral over the IGM in the equation above can be rewritten as

$$\frac{dN_{\text{HII}}^V}{dt} = \dot{N}_{\text{ion}}^{\text{IGM}} - \int_V \alpha n_{\text{HII}} n_{\text{e}} \mathcal{F} dv, \quad (3)$$

where $\mathcal{F} \equiv e^{-\tau_{\text{eff}}}$ is the transmission factor of the diffuse IGM, and τ_{eff} is the effective optical depth to ionizing photons from external sources. We have replaced $N_{\text{HII}}^{\text{IGM}}$ with N_{HII}^V , the number of ionized hydrogen atoms in the comoving volume V , assuming that most of the ionized hydrogen resides in the IGM.

We obtain the time evolution of the mass-weighted ionization fraction, $\langle x_{\text{HII}} \rangle_M$, by dividing both sides of Eq. (3) by V and the mean hydrogen number density $\langle n_{\text{H}} \rangle_V$,

$$\frac{d\langle x_{\text{HII}} \rangle_M}{dt} = \frac{\langle \dot{n}_{\text{ion}} \rangle_V}{\langle n_{\text{H}} \rangle_V} - C_{\text{rec}, \mathcal{F}} \langle \alpha \rangle_V \langle x_{\text{HII}} \rangle_M \langle n_{\text{e}} \rangle_V \langle \mathcal{F} \rangle_V, \quad (4)$$

where

$$C_{\text{rec}, \mathcal{F}} \equiv \frac{\langle \alpha n_{\text{HII}} n_{\text{e}} \mathcal{F} \rangle_V}{\langle \alpha \rangle_V \langle n_{\text{HII}} \rangle_V \langle n_{\text{e}} \rangle_V \langle \mathcal{F} \rangle_V} \quad (5)$$

is the recombination clumping factor. We have used notation for the volumetric average, $\langle X \rangle_V = \int_V X dv / V$, and the mass-weighted average, $\langle X \rangle_M = \int_V \rho_{\text{H}} X dv / \int_V \rho_{\text{H}} dv$, where ρ_{H} is the mass density of hydrogen. We note the relation $\langle x_{\text{HII}} \rangle_M = \langle n_{\text{HII}} \rangle_V / \langle n_{\text{H}} \rangle_V$.

It is helpful to normalize the clumping factor to a fixed temperature and remove the $\langle \mathcal{F} \rangle_V$ term in the denominator for practical use. Then, Eq. (4) becomes

$$\frac{d\langle x_{\text{HII}} \rangle_M}{dt} = \frac{\langle n_{\text{ion}} \rangle_V}{\langle n_{\text{H}} \rangle_V} - C_{\text{norm}, \mathcal{F}} \alpha (10^4 \text{ K}) \langle x_{\text{HII}} \rangle_M \langle n_{\text{e}} \rangle_V \quad (6)$$

with

$$C_{\text{norm}, \mathcal{F}} \equiv \frac{\langle \alpha n_{\text{HII}} n_{\text{e}} \mathcal{F} \rangle_V}{\alpha (10^4 \text{ K}) \langle n_{\text{HII}} \rangle_V \langle n_{\text{e}} \rangle_V} \quad (7)$$

being the normalized clumping factor.

In Sections 3 and 4, we evaluate the clumping factor using cosmological hydrodynamical simulations. We adopt the fitting function for the case B recombination coefficient presented by L. Hui & N. Y. Gnedin (1997), taking into account that the mean free path of ionizing photons is shorter than the Hubble length for $z > 6$ (P. Madau et al. 2024). The effective optical depth is evaluated as $\tau_{\text{eff}} = \frac{1}{2} \bar{\sigma}_{\text{ion}} n_{\text{HI}}^2 / |\nabla n_{\text{HI}}|$ using the gray (spectrum-averaged) ionization cross-section for hydrogen, $\bar{\sigma}_{\text{ion}} \equiv \int_{\nu_{\text{HI}}}^{\nu_{\text{HeII}}} \frac{J_{\nu}}{\nu} \sigma_{\text{H}, \nu} d\nu / \int_{\nu_{\text{HI}}}^{\nu_{\text{HeII}}} \frac{J_{\nu}}{\nu} d\nu$, where the ν_{HI} and ν_{HeII} are the frequencies at the hydrogen Lyman edge and He II ionization edge, respectively. The J_{ν} is the UVB intensity, and $\sigma_{\text{H}, \nu}$ is the photoionization cross-section for hydrogen (A. Rahmati et al. 2013).

3. FULL-BOX SIMULATION

3.1. Method

We generate the initial condition at $z = 99$ using the cosmological initial condition generator MUSIC v1.53³ (O. Hahn & T. Abel 2011). We assume a flat Λ CDM cosmology with cosmological parameters $(\Omega_m, \Omega_\Lambda, \Omega_b, \sigma_8, n_s, h) = (0.3147, 0.6853, 0.0492, 0.8101, 0.9652, 0.6737)$, consistent with the Planck 2018 results (Planck Collaboration et al. 2020). The comoving volume of $(20 h^{-1} \text{ Mpc})^3$ is covered by 1024^3 uniform-resolution grids; the cell size at root level is 29.0 comoving kpc, the particle mass of dark matter is $m_{\text{DM}} = 8.15 \times 10^5 M_\odot$, and the mean mass of the gas cell is $m_{\text{gas,IC}} = 1.51 \times 10^5 M_\odot$.

We perform cosmological hydrodynamical simulations using the adaptive mesh refinement (AMR) code GAMER v2.1.1⁴ (H.-Y. Schive et al. 2018) with the MUSCL-Hancock scheme, the HLLC Riemann solver, and the piecewise linear reconstruction method. The self-gravity of dark matter and baryons is computed

by solving the Poisson equation using the successive-over-relaxation method with the fast Fourier transform method at the base level.

The mesh refinement is allowed to an additional four refinement levels to the root level, and the finest cell size is 1.81 comoving kpc, which is enough to resolve the Jeans length of the cosmic filaments in the IGM. GAMER-2 adopts the so-called block-based AMR structure, and we refine a patch (block) consisting of 8^3 cells into eight patches when either of the following refinement criteria is satisfied: 1) the number of particles in the patch, including dark matter and stars, exceeds 2048, 2) the gas mass of any cell in the patch exceeds $4 m_{\text{gas,IC}}$, or 3) the cell length exceeds one fourth of the local Jeans length of any cell in the patch. The Jeans refinement criterion is applied only to the refinement of levels 2 and 3.

For the treatment of radiative cooling and star formation, we follow the common physics model of the CosmoRun of the AGORA project, as summarized below.

Radiative cooling and the ultraviolet background (UVB) are calculated using the cooling library GRACKLE⁵ (B. D. Smith et al. 2017). We adopt the UVB model by F. Haardt & P. Madau (2012, HM12), which is activated at $z = 15$. Additionally, we apply a floor at the temperature of the cosmic microwave background (CMB). We also apply the non-thermal Jeans pressure floor to prevent artificial fragmentation (J. K. Truelove et al. 1997; J.-h. Kim et al. 2016). A star particle has a mass of more than $6.1 \times 10^4 M_\odot$ at creation and is formed stochastically at a rate of

$$\dot{\rho}_* = \epsilon_* \frac{\rho_{\text{gas}}}{t_{\text{ff}}} \quad (8)$$

when the hydrogen number density exceeds 1 cm^{-3} , where $\epsilon_* = 0.01$ is the star formation efficiency, and $t_{\text{ff}} = \sqrt{3\pi/32G\rho_{\text{gas}}}$ is the local free-fall time.

Unlike AGORA's common physics, we use the non-equilibrium cooling mode that calculates the abundances of electrons, H I, H II, He I, He II, and He III using GRACKLE v3.3. We also use the self-shielding option 3 of GRACKLE, which considers self-shielding in H I and He I using the fitting formula of A. Rahmati et al. (2013), but ignores He II ionization and heating from the UV background.

We evolve the initial condition to $z = 5.5$ with three different UVB intensities. We call the run evolved with the default HM12 UVB intensity the HM12UVB run, and

³ The code's website is <https://www-n.oca.eu/ohahn/MUSIC/index.html>

⁴ The code's website is <https://github.com/gamer-project/gamer>

⁵ The code's website is <https://grackle.readthedocs.io/>

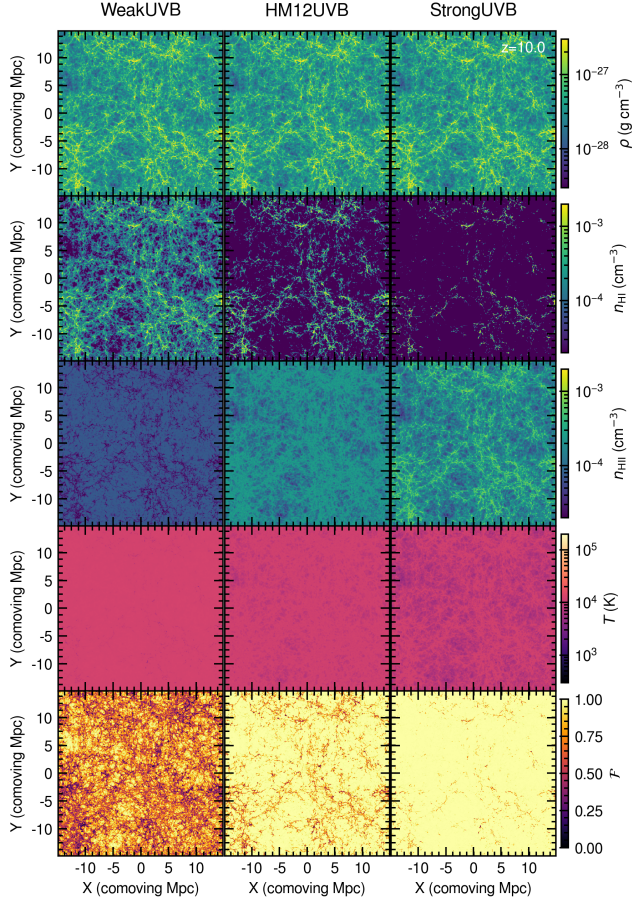


Figure 1. shows slices of the WeakUVB run (left), HM12UVB run (middle), and StrongUVB run (right) at $z = 10$. From top to bottom: gas density, H I number density, H II number density, temperature, and effective transmission factor of ionizing photon.

the runs with three and one-third times the default intensity StrongUVB and WeakUVB runs, respectively.

We note that stellar feedback, including radiative feedback, is not included, and we assume a uniform UV background radiation as an ionizing source.

3.2. Results

Figure 1 shows the slices of the gas density, H I density, H II density, temperature, and effective transmission factor at $z = 10$. The WeakUVB, HM12UVB, and StrongUVB runs exhibit nearly identical density, as they evolve from the same initial condition. The H I density increases for runs with weaker UVB intensity, leading to a corresponding decrease in the effective transmission factor. In contrast, the temperature in the IGM is lower for runs with higher UVB intensities. With stronger UVB, hydrogen is ionized earlier, resulting in reduced photoionization heating at $z = 10$.

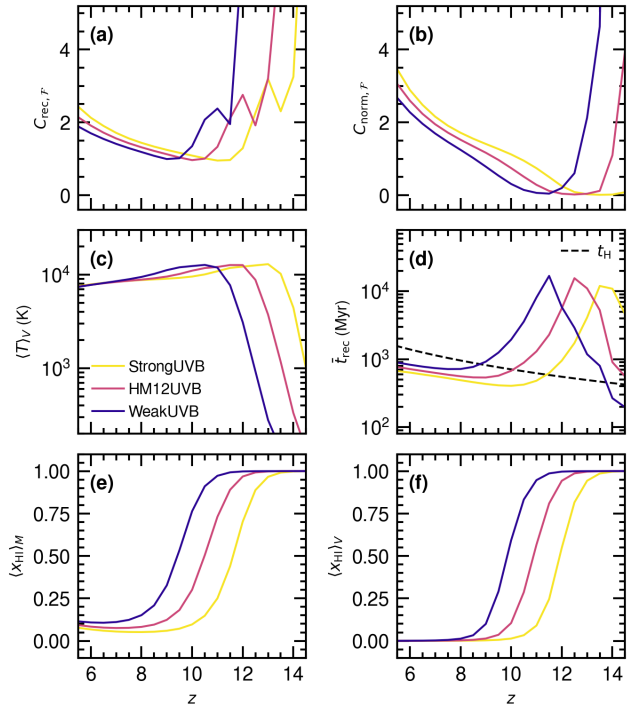


Figure 2. shows redshift evolution of the (a) recombination clumping factor, (b) normalized clumping factor, (c) volume-averaged temperature, (d) mean recombination time, (e) mass-weighted average of the neutral fraction of hydrogen, and (f) volume-weighted average of the neutral fraction of hydrogen. The yellow, magenta, and blue lines are from StrongUVB, HM12UVB, and WeakUVB runs, respectively. The dashed line in the panel (d) indicates the Hubble time.

The top left panel of Figure 2 shows the redshift evolution of the clumping factors from HM12UVB, StrongUVB, and WeakUVB runs. The $C_{\text{rec},\mathcal{F}}$ as a function of redshift shows a V-shape, with the increase toward higher and lower redshift due to a larger clumpiness of the \mathcal{F} field and H II density field, respectively. Stronger UVB intensity causes earlier reionization, shifting the redshift evolution of $C_{\text{rec},\mathcal{F}}$ to a higher redshift.

Normalizing the recombination coefficient and \mathcal{F} , we obtain the normalized clumping factor $C_{\text{norm},\mathcal{F}}$ as shown in the top right panel of Figure 2. The increase in $C_{\text{norm},\mathcal{F}}$ towards a higher redshift is due to a high $\langle \alpha \rangle_V$ caused by the low IGM temperature at high redshift.

The redshift evolution of the volume-averaged temperature is shown in the middle left panel of Figure 2. The temperature in the IGM increases due to photoheating, which raises the temperature of the gas to $> 10^4$ K before the neutral fraction begins to drop significantly.

The middle right panel of Figure 2 shows the redshift evolution of the recombination time scale averaged in

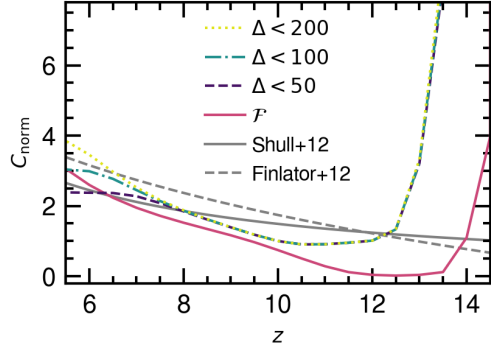


Figure 3. shows redshift evolution of the normalized clumping factor from HM12UVB. The solid line shows the $C_{\text{norm},\mathcal{F}}$, and dashed, dot-dashed, and dotted lines are $C_{\text{norm},\Delta_{\text{th}}}$ with $\Delta_{\text{th}} = 50, 100$, and 200 , respectively. The gray solid and dashed lines display fitting functions from J. M. Shull et al. (2012) and K. Finlator et al. (2012), respectively.

the IGM,

$$\bar{t}_{\text{rec}} = \frac{\langle n_{\text{HII}} \mathcal{F} \rangle_V}{\langle \alpha n_{\text{HII}} n_e \mathcal{F} \rangle_V}. \quad (9)$$

The recombination timescale decreases as reionization proceeds. Comparison with the Hubble time (dashed line) indicates that recombination is insignificant in the early phase of reionization, while it becomes important in the later phase.

The bottom panels of Figure 2 show the mass-weighted and volume-weighted averages of the neutral fraction of hydrogen. They show a similar trend; however, there are differences in the timing of reionization, as we will discuss in Section 3.3. The mass-weighted neutral fraction converges to ~ 0.1 , while the volume-weighted neutral fraction converges to ~ 0 at $z = 5.5$, indicating that dense regions remain neutral, while underdense regions are fully ionized.

Figure 3 compares the redshift evolution of clumping factors obtained using different IGM criteria from the HM12UVB run. The solid magenta line is the $C_{\text{rec},\mathcal{F}}$, as defined in Eq. (5), which is identical to the magenta line in the top left panel of Figure 2. Instead of using \mathcal{F} , one can consider the IGM as the region where the gas overdensity is below a threshold and define the clumping factor as

$$C_{\text{rec},\Delta_{\text{th}}} = \frac{\langle \alpha n_{\text{HII}} n_e \theta(\Delta_{\text{th}} - \Delta) \rangle_V}{\langle \alpha \rangle_V \langle n_{\text{HII}} \rangle_V \langle n_e \rangle_V \langle \theta(\Delta_{\text{th}} - \Delta) \rangle_V}, \quad (10)$$

where θ is the Heaviside step function. Then, the normalized form becomes

$$C_{\text{norm},\Delta_{\text{th}}} = \frac{\langle \alpha n_{\text{HII}} n_e \theta(\Delta_{\text{th}} - \Delta) \rangle_V}{\alpha (10^4 \text{ K}) \langle n_{\text{HII}} \rangle_V \langle n_e \rangle_V}. \quad (11)$$

The dashed, dot-dashed, and dotted lines in Figure 3 are the normalized clumping factors obtained with $\Delta_{\text{th}} =$

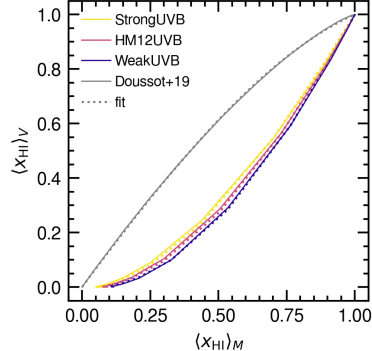


Figure 4. illustrates volume-weighted vs. mass-weighted neutral fraction of hydrogen. The solid lines show the results from our simulations. The gray dot dashed line is the relation taken from the SCORCH II radiation hydrodynamical simulation (A. Doussot et al. 2019). The dotted lines are our fits to our simulations and the SCORCH II results (Eq. (12) and (13)).

50, 100, and 200, respectively. The clumping factors obtained with different IGM criteria show similar redshift evolution at $z < 10$, although $C_{\text{norm},\mathcal{F}}$ is lower than $C_{\text{norm},\Delta_{\text{th}}}$ at $z > 6.5$ because \mathcal{F} excludes self-shielded cells that tend to have a higher recombination rate. Differences in the threshold overdensity Δ_{th} lead to variations in $C_{\text{norm},\Delta_{\text{th}}}$ at $z < 7.5$, with higher thresholds yielding larger clumping factors. We revisit the differences at $z > 10$ later. We also compare our results with fitting functions from J. M. Shull et al. (2012) and K. Finlator et al. (2012), which are shown as gray solid and dashed lines, respectively. We find that our results are consistent within a factor of two with these previous studies at $z < 10$.

To facilitate the application of our results to analytic models, we explore the clumping factor as a function of the neutral fraction of hydrogen, instead of redshift. To begin with, we investigate the relation between the volume-weighted and mass-weighted neutral fractions of hydrogen, as shown in Figure 4. The color dotted lines represent the fit to each simulation result, and the fitting function is expressed as

$$\langle x_{\text{HI}} \rangle_V = \langle x_{\text{HI}} \rangle_M^{3.14 - 0.12z}. \quad (12)$$

The gray solid line represents the $\langle x_{\text{HI}} \rangle_V - \langle x_{\text{HI}} \rangle_M$ relation from the SCORCH II radiation hydrodynamical simulation (A. Doussot et al. 2019), and the gray dotted line illustrates our fit to their result:

$$\langle x_{\text{HI}} \rangle_{V,\text{SCORCH}} = 1.344 \langle x_{\text{HI}} \rangle_M - 0.134 \langle x_{\text{HI}} \rangle_M^2 - 0.211 \langle x_{\text{HI}} \rangle_M^3. \quad (13)$$

Our relation is biased toward higher $\langle x_{\text{HI}} \rangle_M$ because reionization proceeds from low-density regions. The re-

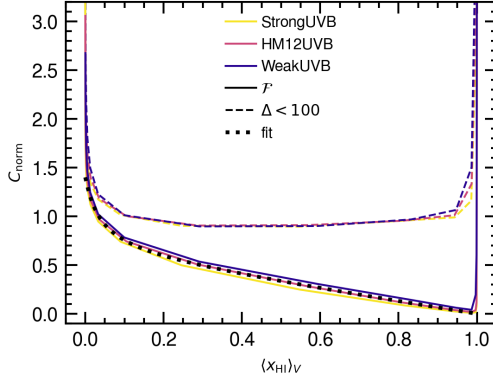


Figure 5. shows the recombination clumping factor as a function of volume-weighted neutral fraction. The solid lines show $C_{\text{norm},\mathcal{F}}$, and the dashed lines show the $C_{\text{norm},\Delta_{\text{th}}}$ with threshold density $\Delta_{\text{th}} = 100$, respectively. The dotted line is the fitting function to $C_{\text{norm},\mathcal{F}}$ (Eq. (14)).

sults from the SCORCH II simulation show an opposite trend, which is due to the inside-out reionization topology caused by ionization from galaxies formed in high-density regions.

Figure 5 shows the the recombination clumping factor as a function of the volume-weighted neutral fraction from our three simulations. The solid lines are $C_{\text{norm},\mathcal{F}}$, and the dashed lines are $C_{\text{norm},\Delta_{\text{th}}}$ with a threshold density $\Delta_{\text{th}} = 100$. Our three simulations yield consistent results for each clumping factor definition as a function of the neutral fraction. This comparison demonstrates the sensitivity of the clumping factor to the IGM definition. The $C_{\text{norm},\mathcal{F}}$ shows a decreasing trend with increasing neutral fraction, which captures the volume fraction of diffuse ionized IGM. The $C_{\text{norm},\Delta_{\text{th}}}$ shows an almost constant trend, indicating that the density threshold definition does not effectively capture the evolution of the diffuse ionized volume fraction. We find $C_{\text{norm},\mathcal{F}} \approx (0.8, 0.3, 0.07)$ at $\langle x_{\text{HI}} \rangle_V = (0.1, 0.5, 0.9)$, which are contrasted with the commonly adopted range $1 \lesssim C \lesssim 5$ (e.g., J. M. Shull et al. 2012; K. Finlator et al. 2012). We fit the $C_{\text{norm},\mathcal{F}}$ with

$$C_{\text{norm},\mathcal{F}} = \frac{0.67\langle x_{\text{HII}} \rangle_V - 0.614\langle x_{\text{HII}} \rangle_V^2}{1.04 - \langle x_{\text{HII}} \rangle_V}, \quad (14)$$

where $\langle x_{\text{HII}} \rangle_V = 1 - \langle x_{\text{HI}} \rangle_V$ is the volume-weighted ionized fraction.

3.3. Discussion

3.3.1. Analytic Model Comparison

To illustrate the usefulness of our fitting functions, we first compare analytic model results with simulation results for the evolution of the neutral hydrogen fraction. We integrate the analytic model equation (6) using the

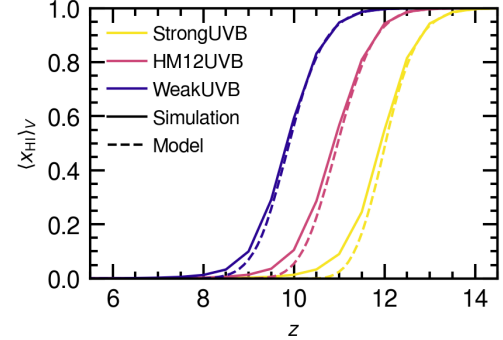


Figure 6. compares the redshift evolution of the volume-weighted neutral fraction of hydrogen from the analytic model and simulations. The solid lines show the simulation result from StrongUVB, HM12UVB, and WeakUVB runs. The dashed lines show the analytic model results using the fitting function for the clumping factor (Eq. (14)) with the ionization rates adopted in each simulation.

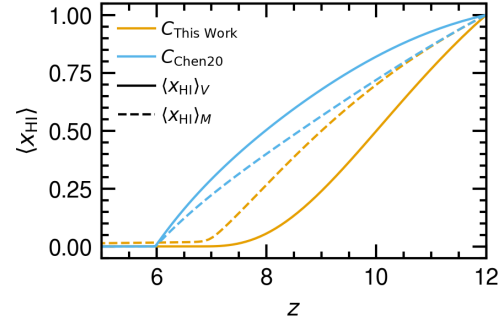


Figure 7. compares the redshift evolution of the neutral fraction of hydrogen from the analytic model using fitting functions to our simulation and SCORCH II simulation results. The orange dashed line shows the $\langle x_{\text{HI}} \rangle_M$ evolution obtained using our fitting functions, and the orange solid line shows the $\langle x_{\text{HI}} \rangle_V$ corresponding to the orange dashed line. The blue dashed line shows the $\langle x_{\text{HI}} \rangle_M$ evolution obtained using the fitting functions from the SCORCH II simulation, and the blue dashed line shows the corresponding $\langle x_{\text{HI}} \rangle_V$.

ionization rate adopted in the simulations and the fitting function of the clumping factor from Eq. (14). We note that the analytic model evolves the $\langle x_{\text{HI}} \rangle_M$, and we use the fitting function for the $C_{\text{norm},\mathcal{F}}$ in combination with Eq. (12) that provides us with the corresponding $\langle x_{\text{HI}} \rangle_V$ for a given $\langle x_{\text{HI}} \rangle_M$.

We compare the redshift evolution of $\langle x_{\text{HI}} \rangle_V$ from the analytic model and simulations in Figure 6. Here, the redshift evolution of $\langle x_{\text{HI}} \rangle_M$ from the analytic model is converted to $\langle x_{\text{HI}} \rangle_V$ using Eq. (12). The analytic model reproduces the simulated redshift evolution of $\langle x_{\text{HI}} \rangle_V$ well when we use our fitting function for the clumping factor.

We further compare fitting functions from our simulations and from the SCORCH II simulations in an analytic model, which is a modified version of the model presented by P. Madau (2017). The model equation is described as

$$\frac{d\langle x_{\text{HII}} \rangle_M}{dt} = \frac{\langle \dot{n}_{\text{ion}} \rangle_V}{\langle n_{\text{H}} \rangle_V (1 + \langle \kappa_{\nu_L}^{\text{LLS}} \rangle / \langle \kappa_{\nu_L}^{\text{IGM}} \rangle)} - C\alpha(10^4 \text{ K}) \left(1 + \frac{Y}{4X}\right) \langle n_{\text{H}} \rangle_V \langle x_{\text{HII}} \rangle_M^2, \quad (15)$$

where $\langle \kappa_{\nu_L}^{\text{LLS}} \rangle = \left[37\{(1+z)/5\}^{-5.4}\right]^{-1} \text{ Mpc}^{-1}$ and $\langle \kappa_{\nu_L}^{\text{IGM}} \rangle = \langle n_{\text{H}} \rangle_V (1 - \langle x_{\text{HII}} \rangle_V) \sigma_L$ are the absorption coefficients at the hydrogen Lyman limit frequency due to Lyman limit systems (LLSs) and the IGM, respectively. Compared to the original model by P. Madau (2017), we have replaced the hydrogen ionized fraction Q in the LHS with $\langle x_{\text{HII}} \rangle_M$, Q in $\kappa_{\nu_L}^{\text{IGM}}$ with $\langle x_{\text{HII}} \rangle_V$, and the recombination term in the RHS with that in our mass-weighted model. We have used the relation $\langle n_e \rangle_V = [1 + Y/(4X)] \langle n_{\text{H}} \rangle_V \langle x_{\text{HI}} \rangle_M$, assuming that helium is singly ionized with the same fraction as ionized hydrogen, with X and Y representing the primordial mass fractions of hydrogen and helium, respectively. We assume a constant ionizing photon production rate per hydrogen atom, $\langle \dot{n}_{\text{ion}} \rangle_V / \langle n_{\text{H}} \rangle_V = 2.9 \text{ Gyr}^{-1}$. We integrate the model equation using the sets of fitting functions for the clumping factor and the $\langle x_{\text{HI}} \rangle_V - \langle x_{\text{HI}} \rangle_M$ relation from our simulations and the SCORCH II simulation, respectively. We rescale the clumping factor for the SCORCH II simulations by N. Chen et al. (2020) by $\alpha(2 \times 10^4 \text{ K}) / \alpha(10^4 \text{ K})$ to account for the different temperature assumed in their formulation.

Figure 7 compares the redshift evolution of $\langle x_{\text{HI}} \rangle_M$ and the corresponding $\langle x_{\text{HI}} \rangle_V$ from the two different fitting functions. The dashed lines show the $\langle x_{\text{HI}} \rangle_M$ evolution obtained using our fitting functions (orange) and the SCORCH II fitting functions (blue), while the solid lines show the corresponding $\langle x_{\text{HI}} \rangle_V$. The outside-in topology in our simulations results in a lower clumping factor at a given neutral fraction compared to the inside-out topology in the SCORCH II simulation, and the reionization process is faster in our fitting functions, with a timing difference of $\Delta z \sim 0.5$ at the middle and $\Delta z \sim 1$ at the end of reionization in the redshift evolution of $\langle x_{\text{HI}} \rangle_M$. The difference in $\langle x_{\text{HI}} \rangle_V - \langle x_{\text{HI}} \rangle_M$ relations amplifies the difference in the reionization history when viewed in terms of volume-weighted neutral fraction, resulting in a timing difference of $\Delta z \sim 2$ at the middle and $\Delta z \sim 1.5$ at the end of reionization.

3.3.2. Implications of Our Clumping Factor Model

As demonstrated above, the clumping factor models predict different reionization histories, depending on the reionization scenario assumed in the underlying simulations. In this work, we have assumed a uniform ionizing background, which is a reasonable approximation when reionization is driven by rare, bright sources such as AGNs (E. Giallongo et al. 2015; P. Madau & F. Haardt 2015; P. Madau et al. 2024; A. Grazian et al. 2024), bright galaxies (M. Sharma et al. 2016; R. P. Naidu et al. 2020; J. Matthee et al. 2022), or population III stars (R. Cen 2003; J. S. B. Wyithe & A. Loeb 2003), as well as for the IGM within an individual ionized bubble, where multiple galaxies work collectively.

The reionization scenarios by bright sources have been challenged by arguments that such sources may not produce enough ionizing photons to complete reionization (e.g., Y. Matsuoka et al. 2018; S. Parsa et al. 2018; D. Jiang et al. 2025). These arguments rely on a simple analytic estimate of the required ionizing photon production rate to balance recombination in the IGM, which is derived from the P. Madau et al. (1999) model, i.e., $\dot{n}_{\text{ion,req}} \approx 10^{50} C [(1+z)/7]^3 \text{ s}^{-1} \text{ cm}^{-3}$, and $1 \lesssim C \lesssim 5$ is a commonly adopted value of the clumping factor suggested from previous simulations (J. M. Shull et al. 2012; K. Finlator et al. 2012). Our $C_{\text{norm},\mathcal{F}} \approx 0.3$ at $\langle x_{\text{HI}} \rangle_V = 0.5$ (see Figure 5) results in an order of magnitude lower $\dot{n}_{\text{ion,req}}$, suggesting that the required ionizing photon production rate may be overestimated in the case of reionization driven by bright sources, especially when the IGM is partially ionized. The lower ionizing photon requirement can also alleviate the tension of He II reionization and IGM temperature history in the reionization scenario with bright sources (A. D’Aloisio et al. 2017; E. Puchwein et al. 2019). Our findings can, therefore, allow for a higher contribution of bright sources to cosmic reionization than previously thought, especially in the early to mid phases of reionization. Although our $C_{\text{norm},\mathcal{F}}$ becomes comparable to the commonly adopted value of $C \sim 3$ when $\langle x_{\text{HI}} \rangle_V \simeq 0$ (see Figure 3), we suggest that external ionizing background by bright sources can assist fainter galaxies in completing reionization.

We have also highlighted the impact of the reionization topology on the $\langle x_{\text{HI}} \rangle_V - \langle x_{\text{HI}} \rangle_M$ relation and the resulting reionization history. The outside-in reionization topology facilitates reionization in terms of volume-weighted neutral fraction, as demonstrated in Figure 7. This finding suggests the necessity of considering the $\langle x_{\text{HI}} \rangle_V - \langle x_{\text{HI}} \rangle_M$ relation in the analytic models, particularly when comparing with observations that probe the volume-weighted neutral fraction, such as the Ly α luminosity function (e.g., C. A. Mason et al. 2018; A.

Hoag et al. 2019; H. Goto et al. 2021) and the 21cm signal (e.g., Z. Abdurashidova et al. 2022). Radiation hydrodynamical simulations are essential for predicting the $\langle x_{\text{HI}} \rangle_V - \langle x_{\text{HI}} \rangle_M$ relation, which can be constrained by observables sensitive to reionization topology, such as the distribution and angular correlation function of Ly α emitters (e.g., E. Sobacchi & A. Mesinger 2015; M. Ouchi et al. 2018; J. Witstok et al. 2024; T.-Y. Lu et al. 2025), the 21 cm power spectrum (e.g., HERA Collaboration et al. 2023; C. D. Nunhokee et al. 2025; F. G. Mertens et al. 2025), and the Ly α damping wing (e.g., H. Umeda et al. 2024).

4. ZOOM-IN SIMULATIONS

Following up on the findings from the large-scale simulations in the previous section, we now investigate the impact of stellar feedback on the recombination clumping factor. We carry out two zoom-in cosmological simulations with and without stellar feedback from an identical initial condition.

4.1. Method

We generate the initial condition at $z = 99$ using MUSIC with the set of parameters taken from the AGORA project⁶ (J.-h. Kim et al. 2014; S. Roca-Fàbrega et al. 2021) tagged 1e12q. We assumed a flat Λ CDM cosmology with cosmological parameters $(\Omega_m, \Omega_\Lambda, \Omega_b, \sigma_8, n_s, h) = (0.272, 0.728, 0.0455, 0.807, 0.961, 0.702)$, consistent with WMAP7/9+SNe+BAO (E. Komatsu et al. 2011; G. Hinshaw et al. 2013). The simulation box of $(60 h^{-1} \text{cMpc})^3$ is covered by root grids of 128^3 with a series of five nested higher-resolution grids; The finest grid level in the initial condition has the equivalent unigrid resolution of 4096^3 . The zoom-in region covered with the finest grids has an ellipsoidal shape that encloses all the dark matter particles that eventually end up within $4R_{\text{vir}}$ of the target halo at $z = 0$. Consequently, at the highest level, the particle mass of dark matter is $m_{\text{DM}} = 2.8 \times 10^5 M_\odot$, and the mean mass of the gas cell is $m_{\text{gas,IC}} = 5.65 \times 10^4 M_\odot$.

We carry out cosmological hydrodynamical simulations using GAMER with the same numerical scheme as in the previous section and AGORA's common subgrid physics model; i.e., we use the equilibrium cooling mode of GRACKLE with the default HM12 UVB model. The hydrogen ionization state is obtained using a table generated with CLOUDY v23.01 (M. Chatzikos et al. 2023) in post-processing. The mesh refinement is allowed to

reach an additional seven refinement levels; thus, the finest refinement level is 12, and its cell size is 163 comoving pc.

Feedback from type II and Ia supernovae (SNe) and asymptotic giant branch (AGB) stars is modeled as presented in Y. Oku et al. (2022) and Y. Oku & K. Nagamine (2024), where the model has been incorporated into the smoothed particle hydrodynamic code GADGET4-OSAKA and is successfully used in the CROCODILE cosmological simulation⁷. We assumed a simple stellar population and generate the metal and energy yield tables for SNe and AGB stars using the chemical evolution library CELIB⁸ (T. R. Saitoh 2017) with the following assumptions. We adopt the Chabrier IMF (G. Chabrier 2003) at solar metallicity and add a log-flat component of massive stars at low metallicities, using the fitting function derived from star cluster formation simulations by S. Chon et al. (2022). We use the type II SN yield model by K. Nomoto et al. (2013), which covers the progenitor mass range of $[13 M_\odot, 40 M_\odot]$. We assume that 30% of those in the progenitor mass range of $[20 M_\odot, 40 M_\odot]$ explode as hypernovae (HNe) when the stellar metallicity is $Z < 10^{-3}$. The HNe have an explosion energy of 10^{52} erg, an order of magnitude larger than normal SNe. The HNe fraction is dropped to 1% at higher metallicities. Considering the possible contributions by SNe from lower-mass progenitors and the missing feedback effects from stellar winds and radiation, we boost the type II SN energy by a factor of three. For type Ia SNe, we assume the power-law-type delay-time distribution (D. Maoz & F. Mannucci 2012) and the element yield model by I. R. Seitenzahl et al. (2013). For AGB stars, we use the element yield table by A. I. Karakas (2010) and C. L. Doherty et al. (2014).

We inject the terminal momentum of SN remnants into the cells surrounding the feedback site, considering the radiative cooling loss on an unresolved scale (T. Kimm & R. Cen 2014; C.-G. Kim & E. C. Ostriker 2017; P. F. Hopkins et al. 2018). We estimate the momentum input from superbubbles formed by clustered SNe using the fitting function of momentum injection per SN, derived from 3D simulations of superbubbles in a variety of density and metallicity environments, as well as different SN explosion intervals by Y. Oku et al. (2022),

$$\hat{p} = 1.75 \times 10^5 M_\odot \text{ km s}^{-1} n_0^{-0.55} \Lambda_{6,-22}^{-0.17}, \quad (16)$$

where $n_0 = n_{\text{H}}/(1 \text{ cm}^{-3})$ is the normalized hydrogen number density, and $\Lambda_{6,-22}^{-0.17} = \max\{1.9 -$

⁶ The project's website is <https://sites.google.com/site/santacruzcomparisonproject/>

⁷ The project's website is <https://sites.google.com/view/crocodilesimulation/home>

⁸ The code's website is <https://bitbucket.org/tsaitoh/celib>

$0.85(Z/0.0194), 1.05\} \times (Z/0.0194) + 10^{-1.33}$ is the value of the cooling function of [R. S. Sutherland & M. A. Dopita \(1993\)](#) at $T = 10^6$ K, normalized by 10^{-22} erg s $^{-1}$ cm 3 . We enforce energy conservation when the increase in kinetic energy due to the momentum input exceeds the SN energy.

We perform two zoom-in simulations with and without stellar feedback, which correspond to the `Cal-3` and `Cal-4` in the calibration steps of the AGORA CosmoRun. We name the run without feedback the `NoFB` run and the run with SN feedback the `SNFB` run.

4.2. Results

Figure 8 shows the projections of density, H I number density, H II number density, temperature, and the effective transmission factor from the `NoFB` and `SNFB` runs at $z = 8$. The stellar mass of the central galaxy at this redshift is $M_* = 2.34 \times 10^9 M_\odot$ and $M_* = 7.84 \times 10^6 M_\odot$ in the `NoFB` and `SNFB` runs, respectively. The feedback effect is most visible in the comparison of the temperature projections between `NoFB` and `SNFB` runs. The high-temperature bubbles ($T \gtrsim 10^5$ K) formed by SN feedback are apparent in the `SNFB` run, which covers ~ 100 kpc around the low-temperature ($T \sim 10^3$ K) cosmic filament. The IGM unaffected by feedback has the equilibrium temperature, $T \sim 10^4$ K. The bubbles are also identified in the density projection in the `SNFB` run, while the `NoFB` run shows a smooth density structure in the IGM. The ionized hydrogen follows the gas distribution, except for the high-density peaks where hydrogen becomes neutral. The ionized hydrogen in the `SNFB` run spreads to a larger distance from the central galaxy compared to the `NoFB` run. The neutral hydrogen is distributed along the cosmic filament, where the ionizing photons are self-shielded ($\mathcal{F} \sim 0$).

Figure 9 shows the radial profiles of density, H II number density, temperature, effective transmission factor, recombination rate, and neutral fraction around the central galaxy at $z = 8$. The `SNFB` run shows a higher density and temperature than the `NoFB` run at $2 \text{ kpc} < r < 100 \text{ kpc}$ due to the galactic outflow driven by SN feedback. The SN feedback also smooths out the neutral hydrogen and increases the \mathcal{F} by $\lesssim 50\%$ at $r < 100 \text{ kpc}$. The recombination rate, given by $\dot{n}_{\text{rec,IGM}} = \alpha n_{\text{HII}} n_e \mathcal{F}$, is higher in the region $2 \text{ kpc} < r < 100 \text{ kpc}$ for the `SNFB` run due to the higher n_{HII} and \mathcal{F} , even though the higher temperature reduces the recombination coefficient. Nonetheless, SN feedback contributes to ionization by heating, thereby reducing the neutral fraction near the center.

The larger recombination rate in the `SNFB` run results in a larger clumping factor on a scale of $R < 100 \text{ kpc}$,

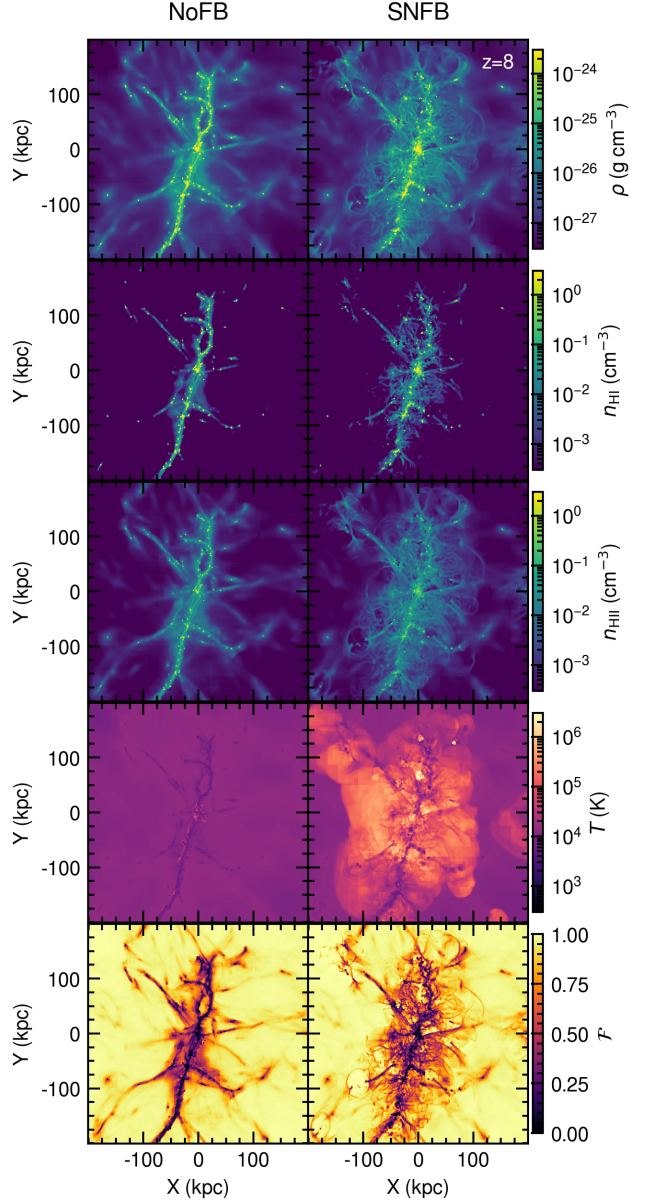


Figure 8. shows density-weighted projections from `NoFB` run (left) and `SNFB` run (right) with projection width and depth of 400 kpc (physical) at $z = 8$. From top to bottom: gas density, H I number density, H II number density, temperature, and effective transmission factor of ionizing photon.

as shown in the top panel of Figure 10. The deviation of the `SNFB` run from the `NoFB` run increases as the feedback effect becomes stronger with the growth of the central galaxy. However, the feedback effect is limited to a physical scale of ~ 100 kpc, and the redshift evolution of the recombination clumping factors from `SNFB` and `NoFB` are comparable on a scale of $\gtrsim 400$ kpc. The middle panel of Figure 10 shows the normalized clumping factors measured in the whole zoom region from `SNFB`

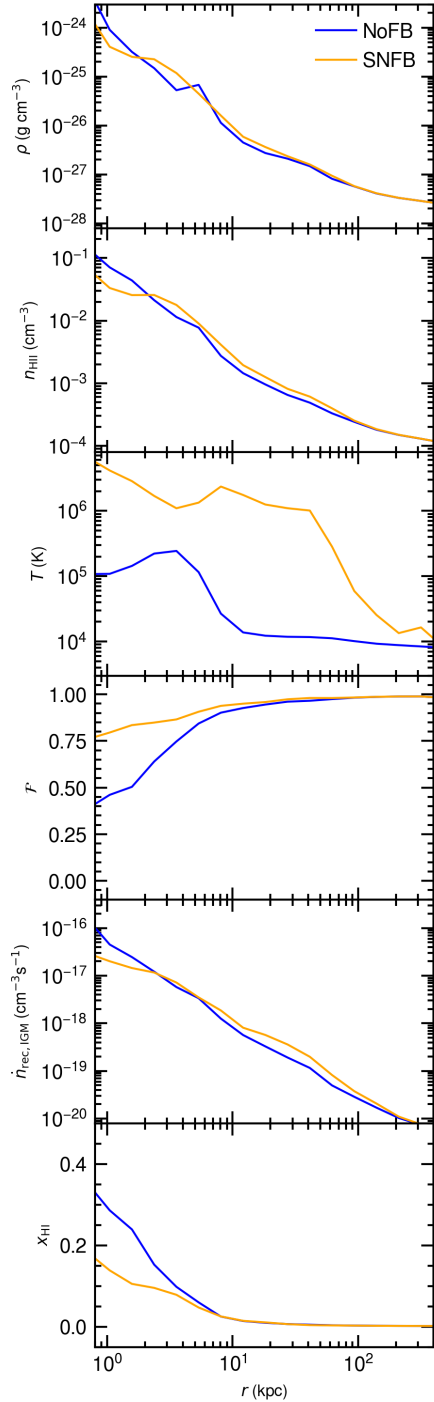


Figure 9. shows spherically averaged quantities as a function of radius in physical kpc around the central galaxy from NoFB run (blue) and SNFB run (orange) at $z = 8$. From top to bottom: density, H II number density, temperature, effective transmission factor, recombination rate, and neutral fraction.

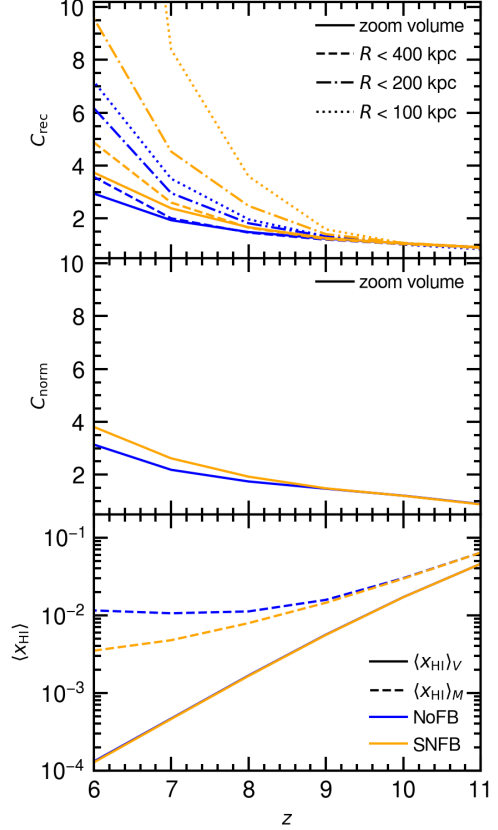


Figure 10. compares the redshift evolutions of clumping factor and neutral fraction from NoFB (blue) and SNFB (orange) runs. Top: The redshift evolution of the recombination clumping factor measured in the zoom volume (solid) and within 400 kpc (dashed), 200 kpc (dash dotted), and 100 kpc (dotted) in physical units around the central galaxy. Middle: The normalized clumping factor measured in zoom volume. Bottom: The volume-weighted neutral fraction (solid) and mass-weighted neutral fraction (dashed) measured in zoom volume.

and NoFB runs, and they also show a comparable redshift evolution, with the difference within $\sim 30\%$. The bottom panel of Figure 10 compares the redshift evolution of volume-weighted and mass-weighted neutral fractions in the zoom volume from SNFB and NoFB runs, which are also similar to each other. The ionization effect by SN feedback appears in $\langle x_{\text{HI}} \rangle_M$ at $z < 9$, while the $\langle x_{\text{HI}} \rangle_V$ shows almost identical evolution between the two runs, which also indicates that the feedback effect is limited to a small volume around the galaxy.

4.3. Discussion

We find that the SN feedback has two competing effects on reionization, i.e., enhancing recombination by increasing the density of ionized gas, while facilitating ionization by heating the gas. Our finding of the SN

feedback effect of boosting the clumping factor is consistent with K. Finlator et al. (2012), who reported that galactic winds increase the clumping factor by less than 30% using cosmological radiation smoothed particle hydrodynamics simulations. Our analysis further reveals that the spatial scale of the feedback effect is limited to ~ 100 kpc around the galaxy, using high-resolution zoom-in AMR simulations.

We also find that SN feedback increases the transmission factor \mathcal{F} , suggesting that feedback can help ionizing photons escape from galaxies, which is consistent with previous simulation studies (e.g., T. Kimm & R. Cen 2014; M. Trebitsch et al. 2017; R. Cen 2020; X. Ma et al. 2020). Recent observational studies suggest that radiation feedback from young stars before SN explosions plays a more important role in creating low-density channels for ionizing photons to escape from galaxies (O. Bait et al. 2024; S. R. Flury et al. 2025; C. A. Carr et al. 2025). Our results do not conflict with these studies, and we find that SN-driven outflows form opaque shells, as can be seen in Figure 8, which can block ionizing photons from escaping to the IGM. From a comparison of our controlled simulations with and without SN feedback, we suggest that the SN feedback prepares a favorable condition for radiation feedback, facilitating photon escape by reducing the gas density and neutral fraction in the ISM and inner CGM.

5. CONCLUSION

We have investigated the recombination clumping factor of the diffuse IGM during cosmic reionization using a set of cosmological hydrodynamical simulations powered by the AMR code GAMER-2 with a uniform UV background radiation. Our definition of the clumping factor is derived from the mass-weighted reionization model with an IGM criterion based on the effective transmission factor of ionizing photons. We have performed three large-scale simulations with different UVB intensities and examined the clumping factor as a function of the neutral fraction of hydrogen. We have also performed two zoom-in simulations with and without SN feedback to study the impact of stellar feedback on the clumping factor. Our main findings are summarized as follows:

1. The recombination clumping factor, based on our IGM definition utilizing the effective transmission factor, $C_{\text{norm},\mathcal{F}}$, exhibits comparable redshift evolution to that defined using an overdensity threshold, $C_{\text{norm},\Delta_{\text{th}}}$, and aligns with previous studies at $z < 10$ in the HM12UVB run, wherein the IGM is predominantly ionized (see Figure 3). However, $C_{\text{norm},\mathcal{F}}$ is significantly lower than $C_{\text{norm},\Delta_{\text{th}}=100}$

when the IGM is partially ionized because \mathcal{F} excludes self-shielded high-density cells that tend to have a higher recombination rate. The clumping factor $C_{\text{norm},\mathcal{F}}$ is reduced to ≈ 0.3 at $\langle x_{\text{HI}} \rangle_V = 0.5$ (see Figure 5), which is an order of magnitude lower compared to commonly adopted values of $1 \lesssim C \lesssim 5$. We provide fitting functions for $C_{\text{norm},\mathcal{F}}$ as a function of the volume-weighted neutral fraction of hydrogen in Eq. (14).

2. The relation between volume-weighted and mass-weighted neutral fractions of hydrogen depends on the reionization topology, and it significantly affects the reionization history predicted by analytic models. The outside-in reionization topology in our simulations results in a higher volume-weighted neutral fraction at a given mass-weighted neutral fraction, compared to the SCORCH II radiation hydrodynamical simulation (see Figure 4). We provide fitting functions for the relation from our simulations in Eq. (12). We have demonstrated that the difference in the $\langle x_{\text{HI}} \rangle_V - \langle x_{\text{HI}} \rangle_M$ relation amplifies the difference in the reionization history to $\Delta z \sim 2$ when viewed in terms of the volume-weighted neutral fraction in the modified analytic model by P. Madau (2017), which distinguishes between the volume-weighted and mass-weighted neutral fractions (see Figure 7).
3. The SN feedback has two competing effects on reionization, i.e., enhancing recombination by increasing the density of ionized gas, while facilitating ionization by heating the gas and reducing the neutral fraction. The feedback effect is limited to a physical scale of ~ 100 kpc in our simulated galaxy (see Figure 9), and the redshift evolution of the recombination clumping factors from simulations with and without SN feedback is comparable on a scale of $\gtrsim 400$ kpc (see Figure 10). In comparison between zoom-in simulations with and without SN feedback, we suggest that the SN feedback prepares a favorable condition for radiation feedback, facilitating photon escape by reducing the gas density and neutral fraction in the ISM and inner CGM.

The variation of $\Delta z \sim 2$ in the reionization timing predicted by different clumping factor models highlights the necessity of an accurate model of the clumping factor and the $\langle x_{\text{HI}} \rangle_V - \langle x_{\text{HI}} \rangle_M$ relation in analytic models of reionization. Our AMR simulations offer high resolution and improve the estimate of clumpiness in the IGM, but they are limited by the assumption of a uniform UV

background radiation, which is a reasonable approximation when reionization is driven by rare, bright sources, or for the IGM within an individual ionized bubble, where multiple galaxies work collectively. Cosmological radiation hydrodynamical simulations, along with further analysis using a physical definition of the diffuse IGM, are essential for providing accurate models of the recombination clumping factor and the $\langle x_{\text{HI}} \rangle_V - \langle x_{\text{HI}} \rangle_M$ relation. They depend on the nature of ionizing sources, and further investigations using simulations with different reionization scenarios are necessary to fully understand their impact on the reionization history. Obser-

vations that can probe the reionization topology, such as the angular correlation function of Ly α emitters, the 21 cm power spectrum, and the Ly α damping wing, provide valuable constraints on these models.

ACKNOWLEDGMENTS

This work is supported in part by the National Key Research and Development Program of China and the Zhejiang Provincial Top-Level Research Support Program. The analysis presented in this article was carried out on the SilkRiver Supercomputer of Zhejiang University.

REFERENCES

Abdurashidova, Z., Aguirre, J. E., Alexander, P., et al. 2022, ApJ, 924, 51, doi: [10.3847/1538-4357/ac2ffc](https://doi.org/10.3847/1538-4357/ac2ffc)

Bait, O., Borthakur, S., Schaerer, D., et al. 2024, A&A, 688, A198, doi: [10.1051/0004-6361/202348416](https://doi.org/10.1051/0004-6361/202348416)

Carr, C. A., Cen, R., Scarlata, C., et al. 2025, ApJ, 982, 137, doi: [10.3847/1538-4357/adb72f](https://doi.org/10.3847/1538-4357/adb72f)

Cen, R. 2003, ApJ, 591, 12, doi: [10.1086/375217](https://doi.org/10.1086/375217)

Cen, R. 2020, ApJL, 889, L22, doi: [10.3847/2041-8213/ab6560](https://doi.org/10.3847/2041-8213/ab6560)

Chabrier, G. 2003, PASP, 115, 763, doi: [10.1086/376392](https://doi.org/10.1086/376392)

Chatzikos, M., Bianchi, S., Camilloni, F., et al. 2023, RMxAA, 59, 327, doi: [10.22201/ia.01851101p.2023.59.02.12](https://doi.org/10.22201/ia.01851101p.2023.59.02.12)

Chen, N., Doussot, A., Trac, H., & Cen, R. 2020, ApJ, 905, 132, doi: [10.3847/1538-4357/abc890](https://doi.org/10.3847/1538-4357/abc890)

Chon, S., Ono, H., Omukai, K., & Schneider, R. 2022, MNRAS, 514, 4639, doi: [10.1093/mnras/stac1549](https://doi.org/10.1093/mnras/stac1549)

D'Aloisio, A., Upton Sanderbeck, P. R., McQuinn, M., Trac, H., & Shapiro, P. R. 2017, MNRAS, 468, 4691, doi: [10.1093/mnras/stx711](https://doi.org/10.1093/mnras/stx711)

Doherty, C. L., Gil-Pons, P., Lau, H. H. B., Lattanzio, J. C., & Siess, L. 2014, MNRAS, 437, 195, doi: [10.1093/mnras/stt1877](https://doi.org/10.1093/mnras/stt1877)

Doussot, A., Trac, H., & Cen, R. 2019, ApJ, 870, 18, doi: [10.3847/1538-4357/aaef75](https://doi.org/10.3847/1538-4357/aaef75)

Finlator, K., Oh, S. P., Özel, F., & Davé, R. 2012, MNRAS, 427, 2464, doi: [10.1111/j.1365-2966.2012.22114.x](https://doi.org/10.1111/j.1365-2966.2012.22114.x)

Flury, S. R., Jaskot, A. E., Saldana-Lopez, A., et al. 2025, ApJ, 985, 128, doi: [10.3847/1538-4357/adc305](https://doi.org/10.3847/1538-4357/adc305)

Furlanetto, S. R., & Oh, S. P. 2005, MNRAS, 363, 1031, doi: [10.1111/j.1365-2966.2005.09505.x](https://doi.org/10.1111/j.1365-2966.2005.09505.x)

Furlanetto, S. R., Zaldarriaga, M., & Hernquist, L. 2004, ApJ, 613, 1, doi: [10.1086/423025](https://doi.org/10.1086/423025)

Giallongo, E., Grazian, A., Fiore, F., et al. 2015, A&A, 578, A83, doi: [10.1051/0004-6361/201425334](https://doi.org/10.1051/0004-6361/201425334)

Gnedin, N. Y., & Madau, P. 2022, Living Reviews in Computational Astrophysics, 8, 3, doi: [10.1007/s41115-022-00015-5](https://doi.org/10.1007/s41115-022-00015-5)

Gnedin, N. Y., & Ostriker, J. P. 1997, ApJ, 486, 581, doi: [10.1086/304548](https://doi.org/10.1086/304548)

Goto, H., Shimasaku, K., Yamanaka, S., et al. 2021, ApJ, 923, 229, doi: [10.3847/1538-4357/ac308b](https://doi.org/10.3847/1538-4357/ac308b)

Grazian, A., Giallongo, E., Boutsia, K., et al. 2024, ApJ, 974, 84, doi: [10.3847/1538-4357/ad6980](https://doi.org/10.3847/1538-4357/ad6980)

Haardt, F., & Madau, P. 2012, ApJ, 746, 125, doi: [10.1088/0004-637X/746/2/125](https://doi.org/10.1088/0004-637X/746/2/125)

Hahn, O., & Abel, T. 2011, MNRAS, 415, 2101, doi: [10.1111/j.1365-2966.2011.18820.x](https://doi.org/10.1111/j.1365-2966.2011.18820.x)

HERA Collaboration, Abdurashidova, Z., Adams, T., et al. 2023, ApJ, 945, 124, doi: [10.3847/1538-4357/acaf50](https://doi.org/10.3847/1538-4357/acaf50)

Hinshaw, G., Larson, D., Komatsu, E., et al. 2013, ApJS, 208, 19, doi: [10.1088/0067-0049/208/2/19](https://doi.org/10.1088/0067-0049/208/2/19)

Hoag, A., Bradač, M., Huang, K., et al. 2019, ApJ, 878, 12, doi: [10.3847/1538-4357/ab1de7](https://doi.org/10.3847/1538-4357/ab1de7)

Hopkins, P. F., Wetzel, A., Kereš, D., et al. 2018, MNRAS, 477, 1578, doi: [10.1093/mnras/sty674](https://doi.org/10.1093/mnras/sty674)

Hui, L., & Gnedin, N. Y. 1997, MNRAS, 292, 27, doi: [10.1093/mnras/292.1.27](https://doi.org/10.1093/mnras/292.1.27)

Jiang, D., Jiang, L., Sun, S., Liu, W., & Fu, S. 2025, Nature Astronomy, doi: [10.1038/s41550-025-02676-7](https://doi.org/10.1038/s41550-025-02676-7)

Kannan, R., Garaldi, E., Smith, A., et al. 2022, MNRAS, 511, 4005, doi: [10.1093/mnras/stab3710](https://doi.org/10.1093/mnras/stab3710)

Karakas, A. I. 2010, MNRAS, 403, 1413, doi: [10.1111/j.1365-2966.2009.16198.x](https://doi.org/10.1111/j.1365-2966.2009.16198.x)

Kaurov, A. A., & Gnedin, N. Y. 2015, ApJ, 810, 154, doi: [10.1088/0004-637X/810/2/154](https://doi.org/10.1088/0004-637X/810/2/154)

Kim, C.-G., & Ostriker, E. C. 2017, ApJ, 846, 133, doi: [10.3847/1538-4357/aa8599](https://doi.org/10.3847/1538-4357/aa8599)

Kim, J.-h., Abel, T., Agertz, O., et al. 2014, ApJS, 210, 14, doi: [10.1088/0067-0049/210/1/14](https://doi.org/10.1088/0067-0049/210/1/14)

Kim, J.-h., Agertz, O., Teyssier, R., et al. 2016, *ApJ*, 833, 202, doi: [10.3847/1538-4357/833/2/202](https://doi.org/10.3847/1538-4357/833/2/202)

Kimm, T., & Cen, R. 2014, *ApJ*, 788, 121, doi: [10.1088/0004-637X/788/2/121](https://doi.org/10.1088/0004-637X/788/2/121)

Kohler, K., Gnedin, N. Y., & Hamilton, A. J. S. 2007, *ApJ*, 657, 15, doi: [10.1086/509907](https://doi.org/10.1086/509907)

Komatsu, E., Smith, K. M., Dunkley, J., et al. 2011, *ApJS*, 192, 18, doi: [10.1088/0067-0049/192/2/18](https://doi.org/10.1088/0067-0049/192/2/18)

Lu, T.-Y., Mason, C. A., Mesinger, A., et al. 2025, *A&A*, 697, A69, doi: [10.1051/0004-6361/202452912](https://doi.org/10.1051/0004-6361/202452912)

Ma, X., Quataert, E., Wetzel, A., et al. 2020, *MNRAS*, 498, 2001, doi: [10.1093/mnras/staa2404](https://doi.org/10.1093/mnras/staa2404)

Madau, P. 2017, *ApJ*, 851, 50, doi: [10.3847/1538-4357/aa9715](https://doi.org/10.3847/1538-4357/aa9715)

Madau, P., Giallongo, E., Grazian, A., & Haardt, F. 2024, *ApJ*, 971, 75, doi: [10.3847/1538-4357/ad5ce8](https://doi.org/10.3847/1538-4357/ad5ce8)

Madau, P., & Haardt, F. 2015, *ApJL*, 813, L8, doi: [10.1088/2041-8205/813/1/L8](https://doi.org/10.1088/2041-8205/813/1/L8)

Madau, P., Haardt, F., & Rees, M. J. 1999, *ApJ*, 514, 648, doi: [10.1086/306975](https://doi.org/10.1086/306975)

Maoz, D., & Mannucci, F. 2012, *PASA*, 29, 447, doi: [10.1071/AS11052](https://doi.org/10.1071/AS11052)

Mason, C. A., Treu, T., Dijkstra, M., et al. 2018, *ApJ*, 856, 2, doi: [10.3847/1538-4357/aab0a7](https://doi.org/10.3847/1538-4357/aab0a7)

Matsuoka, Y., Strauss, M. A., Kashikawa, N., et al. 2018, *ApJ*, 869, 150, doi: [10.3847/1538-4357/aaeee7a](https://doi.org/10.3847/1538-4357/aaeee7a)

Matthee, J., Naidu, R. P., Pezzulli, G., et al. 2022, *MNRAS*, 512, 5960, doi: [10.1093/mnras/stac801](https://doi.org/10.1093/mnras/stac801)

Mertens, F. G., Mevius, M., Koopmans, L. V. E., et al. 2025, *A&A*, 698, A186, doi: [10.1051/0004-6361/202554158](https://doi.org/10.1051/0004-6361/202554158)

Miralda-Escudé, J., Haehnelt, M., & Rees, M. J. 2000, *ApJ*, 530, 1, doi: [10.1086/308330](https://doi.org/10.1086/308330)

Naidu, R. P., Tacchella, S., Mason, C. A., et al. 2020, *ApJ*, 892, 109, doi: [10.3847/1538-4357/ab7cc9](https://doi.org/10.3847/1538-4357/ab7cc9)

Nomoto, K., Kobayashi, C., & Tominaga, N. 2013, *ARA&A*, 51, 457, doi: [10.1146/annurev-astro-082812-140956](https://doi.org/10.1146/annurev-astro-082812-140956)

Nunhokee, C. D., Null, D., Trott, C. M., et al. 2025, *ApJ*, 989, 57, doi: [10.3847/1538-4357/adda45](https://doi.org/10.3847/1538-4357/adda45)

Oku, Y., & Nagamine, K. 2024, *ApJ*, 975, 183, doi: [10.3847/1538-4357/ad77d3](https://doi.org/10.3847/1538-4357/ad77d3)

Oku, Y., Tomida, K., Nagamine, K., Shimizu, I., & Cen, R. 2022, *ApJS*, 262, 9, doi: [10.3847/1538-4365/ac77ff](https://doi.org/10.3847/1538-4365/ac77ff)

Ouchi, M., Harikane, Y., Shibuya, T., et al. 2018, *PASJ*, 70, S13, doi: [10.1093/pasj/psx074](https://doi.org/10.1093/pasj/psx074)

Parsa, S., Dunlop, J. S., & McLure, R. J. 2018, *MNRAS*, 474, 2904, doi: [10.1093/mnras/stx2887](https://doi.org/10.1093/mnras/stx2887)

Pawlik, A. H., Schaye, J., & van Scherpenzeel, E. 2009, *MNRAS*, 394, 1812, doi: [10.1111/j.1365-2966.2009.14486.x](https://doi.org/10.1111/j.1365-2966.2009.14486.x)

Planck Collaboration, Aghanim, N., Akrami, Y., et al. 2020, *A&A*, 641, A6, doi: [10.1051/0004-6361/201833910](https://doi.org/10.1051/0004-6361/201833910)

Puchwein, E., Haardt, F., Haehnelt, M. G., & Madau, P. 2019, *MNRAS*, 485, 47, doi: [10.1093/mnras/stz222](https://doi.org/10.1093/mnras/stz222)

Rahmati, A., Pawlik, A. H., Raičević, M., & Schaye, J. 2013, *MNRAS*, 430, 2427, doi: [10.1093/mnras/stt066](https://doi.org/10.1093/mnras/stt066)

Robertson, B. E. 2022, *ARA&A*, 60, 121, doi: [10.1146/annurev-astro-120221-044656](https://doi.org/10.1146/annurev-astro-120221-044656)

Roca-Fàbrega, S., Kim, J.-H., Hausammann, L., et al. 2021, *ApJ*, 917, 64, doi: [10.3847/1538-4357/ac088a](https://doi.org/10.3847/1538-4357/ac088a)

Saitoh, T. R. 2017, *AJ*, 153, 85, doi: [10.3847/1538-3881/153/2/85](https://doi.org/10.3847/1538-3881/153/2/85)

Schive, H.-Y., ZuHone, J. A., Goldbaum, N. J., et al. 2018, *MNRAS*, 481, 4815, doi: [10.1093/mnras/sty2586](https://doi.org/10.1093/mnras/sty2586)

Seitenzahl, I. R., Ciaraldi-Schoolmann, F., Röpke, F. K., et al. 2013, *MNRAS*, 429, 1156, doi: [10.1093/mnras/sts402](https://doi.org/10.1093/mnras/sts402)

Sharma, M., Theuns, T., Frenk, C., et al. 2016, *MNRAS*, 458, L94, doi: [10.1093/mnrasl/slw021](https://doi.org/10.1093/mnrasl/slw021)

Shull, J. M., Harness, A., Trenti, M., & Smith, B. D. 2012, *ApJ*, 747, 100, doi: [10.1088/0004-637X/747/2/100](https://doi.org/10.1088/0004-637X/747/2/100)

Smith, B. D., Bryan, G. L., Glover, S. C. O., et al. 2017, *MNRAS*, 466, 2217, doi: [10.1093/mnras/stw3291](https://doi.org/10.1093/mnras/stw3291)

So, G. C., Norman, M. L., Reynolds, D. R., & Wise, J. H. 2014, *ApJ*, 789, 149, doi: [10.1088/0004-637X/789/2/149](https://doi.org/10.1088/0004-637X/789/2/149)

Sobacchi, E., & Mesinger, A. 2015, *MNRAS*, 453, 1843, doi: [10.1093/mnras/stv1751](https://doi.org/10.1093/mnras/stv1751)

Sutherland, R. S., & Dopita, M. A. 1993, *ApJS*, 88, 253, doi: [10.1086/191823](https://doi.org/10.1086/191823)

Trac, H., & Cen, R. 2007, *ApJ*, 671, 1, doi: [10.1086/522566](https://doi.org/10.1086/522566)

Trebitsch, M., Blaizot, J., Rosdahl, J., Devriendt, J., & Slyz, A. 2017, *MNRAS*, 470, 224, doi: [10.1093/mnras/stx1060](https://doi.org/10.1093/mnras/stx1060)

Truelove, J. K., Klein, R. I., McKee, C. F., et al. 1997, *ApJL*, 489, L179, doi: [10.1086/310975](https://doi.org/10.1086/310975)

Ueda, H., Ouchi, M., Nakajima, K., et al. 2024, *ApJ*, 971, 124, doi: [10.3847/1538-4357/ad554e](https://doi.org/10.3847/1538-4357/ad554e)

Witstok, J., Smit, R., Saxena, A., et al. 2024, *A&A*, 682, A40, doi: [10.1051/0004-6361/202347176](https://doi.org/10.1051/0004-6361/202347176)

Wyithe, J. S. B., & Loeb, A. 2003, *ApJL*, 588, L69, doi: [10.1086/375682](https://doi.org/10.1086/375682)